Targeting CD146 with a ^{64}Cu-labeled antibody enables in vivo immunoPET imaging of high-grade gliomas

Yunan Yang[a,b,1], Reinier Hernandez[c,1], Jun Rao[b], Li Yin[b], Yazhuo Qu[b], Jinrong Wu[b], Christopher G. England[c], Stephen A. Graves[c], Christina M. Lewis[c], Pu Wang[b], Mary E. Meyerand[c], Robert J. Nickles[c], Xiu-wu Bian[b,2], and Weibo Cai[a,c,d,2]

[a]Department of Radiology, University of Wisconsin-Madison, Madison, WI 53705; [b]Department of Pathology, Southwest Hospital, Third Military Medical University, Chongqing, China 400038; [c]Department of Medical Physics, University of Wisconsin-Madison, Madison, WI 53705; and [d]University of Wisconsin Carbone Cancer Center, Madison, WI 53705

Edited by Michael E. Phelps, University of California, Los Angeles, CA, and approved October 14, 2015 (received for review February 8, 2015)

Given the highly heterogeneous character of brain malignancies and the associated implication for its proper diagnosis and treatment, finding biomarkers that better characterize this disease from a molecular standpoint is imperative. In this study, we evaluated CD146 as a potential molecular target for diagnosis and targeted therapy of glioblastoma multiforme (GBM), the most common and lethal brain malignancy. YY146, an anti-CD146 monoclonal antibody, was generated and radiolabeled for noninvasive positron-emission tomography (PET) imaging of orthotopic GBM models. ^{64}Cu-labeled YY146 preferentially accumulated in the tumors of mice bearing U87MG xenografts, which allowed the acquisition of high-contrast PET images of small tumor nodules (~2 mm). Additionally, we found that tumor uptake correlated with the levels of CD146 expression in a highly specific manner. We also explored the potential therapeutic effects of YY146 on the cancer stem cell (CSC) and epithelial-to-mesenchymal (EMT) properties of U87MG cells, demonstrating that YY146 can mitigate those aggressive phenotypes. Using YY146 as the primary antibody, we performed histological studies of World Health Organization (WHO) grades I through IV primary gliomas. The positive correlation found between CD146-positive staining and high tumor grade ($\chi^2 = 9.028$; $P = 0.029$) concurred with the GBM data available in The Cancer Genome Atlas (TCGA) and validated the clinical value of YY146. In addition, we demonstrate that YY146 can be used to detect CD146 in various cancer cell lines and human resected tumor tissues of multiple other tumor types (gastric, ovarian, liver, and lung), indicating a broad applicability of YY146 in solid tumors.

CD146 | epithelial-mesenchymal transition | positron emission tomography | glioblastoma multiforme | cancer stem cells

About 23,000 new cases of brain and central nervous system tumors are expected to be diagnosed in 2015 in the United States alone (1). More importantly, 15,320 patients will likely die of brain cancer by the end of the year, the majority of them due to malignant tumors types (1, 2). Glioblastoma multiforme (GBM) is the most common brain malignancy, accounting for more than 45% of all primary malignant brain tumors. Incidence rates of GBM increase with age, peaking at ages between 75 and 84; as a result, the number of glioblastoma cases is expected to increase in the United States due to population aging (3). Amid the significant efforts devoted to find effective therapeutic strategies for the treatment of GBM, it remains an incurable disease with a dismal 5-y survival rate of only 5%.

Recent understanding of the complex molecular mechanisms underlying GBM's pathogenesis has revealed the considerable heterogeneity inherent to the disease and has led to the emergence of several promising, patient-tailored therapies (3, 4). However, these therapies benefit only a specific subset of patients and almost invariably need the implementation of combinatorial regimes that simultaneously target several tumor-associated pathways to avoid tumor recurrence and rapid development of resistance. Therefore, it is critical to find new relevant GBM molecular signatures that allow for better patient stratification into specific molecular subtypes and the design of effective targeted therapeutic agents. The creation of The Cancer Genome Atlas (TCGA), and with it the availability of invaluable cancer genome data, has been instrumental in creating the opportunity for researchers to explore the genomic profile of several malignancies and identify new targets that might allow the emergence of novel diagnostics and therapeutic paradigms. GBM was the first malignancy incorporated to TCGA for which extensive genomic and matched phenotypical and clinical data are available.

We identified CD146 as a promising diagnosis and therapeutic target for GBM. Subsequent analysis of the TCGA data revealed a statistically significant correlation between the expression of CD146 and decreased disease-free survival and overall survival in glioblastoma patients (Fig. S1). Thus, we devoted our efforts to validate CD146 as a target for noninvasive diagnosis and stratification of GBMs and to evaluate its potential as a therapeutic target. CD146, also known as MCAM, Mel-CAM, MUC18, or S-endo1, was first identified as a tumor progression and metastasis marker in malignant melanomas (5, 6). The major roles of CD146 have been associated with intercellular and cell-matrix adhesion. However, its involvement in several other processes, including development, cell migration, signal transduction, stem cell differentiation, immune response, angiogenesis, and, more

Significance

Unfortunately, current practices for diagnosis and treatment of glioblastoma have failed to improve overall patient survival, which has galvanized the emergence of novel strategies based on targeting tumor-specific antigens. Herein, we show for the first time, to our knowledge, that CD146 is a promising target for noninvasive in vivo imaging and targeted therapy of glioblastoma. We developed a ^{64}Cu-radiolabeled anti-CD146 antibody (YY146) that allowed the sensitive and specific detection of subcutaneous and orthotopic brain tumors using positron emission tomography. Additionally, YY146 showed therapeutic effects on U87MG brain cancer cells and was able to preferentially stain human resected high-grade glioma tumors. These findings indicate the clinical relevance of our antibody and its potential role in patient diagnosis, stratification, and targeted therapy.

Author contributions: Y.Y., R.H., M.E.M., X.B., and W.C. designed research; Y.Y., R.H., J.R., L.Y., Y.Q., J.W., C.G.E., S.A.G., and C.M.L. performed research; Y.Y., R.J.N., and X.B. contributed new reagents/analytic tools; Y.Y., R.H., C.G.E., P.W., and X.B. analyzed data; and R.H., C.G.E., and W.C. wrote the paper.

The authors declare no conflict of interest.

This article is a PNAS Direct Submission.

[1]Y.Y. and R.H. contributed equally to this work.

[2]To whom correspondence may be addressed. Email: wcai@uwhealth.org or bianxiuwu@263.net.

This article contains supporting information online at www.pnas.org/lookup/suppl/doi:10.1073/pnas.1502648112/-/DCSupplemental.

recently, induction of epithelial-mesenchymal transition (EMT), has also been documented (7, 8). Despite the copious body of data describing the expression of CD146 in a myriad of cancers, noninvasive in vivo molecular imaging of CD146 expression has remained unexplored.

Molecular imaging techniques such as positron emission tomography (PET) and fluorescence imaging are becoming indispensable tools to study tumor biology in a clinical setting (9). ImmunoPET, which combines the excellent sensitivity and quantification capabilities of PET with monoclonal antibodies' (mAbs') exquisite binding affinity and specificity for their cognate antigen, is one of the most valuable techniques (10, 11). In this study, we used an improved method to produce YY146, an mAb against human CD146, which we implemented as an immunoPET agent for noninvasive in vivo imaging of CD146 expression in an orthotopic GBM mouse model. We further investigated how CD146 expression associates with several stem cell-like and mesenchymal cell traits in tumor cells and determined the ability of YY146 to actuate preferentially on cell subpopulations presenting these aggressive phenotypes. Finally, histological analysis of different WHO grade human brain tumor tissue samples confirmed the clinical relevance of CD146 for diagnosis and stratification of high-grade glioma patients and suggested its feasibility as a target for YY146-based targeted therapies (e.g., YY146 alone or in combination with other drugs, radioimmunotherapy, antibody-drug conjugates, etc.).

Results

Antibody Production and in Vitro Cell Screening. To generate anti-human CD146 mAbs, we adopted a fast immunization approach that consisted of the preparation of cell hybridomas from B cells harvested from the popliteal lymph nodes of mice immunized with CD146. Our mAb production methodology significantly improved standard protocols by reducing the average production time in half (Fig. 1*A*). Aided by ELISA screenings and SDS/PAGE, we selected the five hybridoma clones with the highest immunoreactivity toward CD146 (Fig. S2 *A* and *B*). Immunofluorescence staining of malignant human melanoma cells (A375), known to overexpress CD146, revealed YY146 (the fifth mAb clone) as the mAb with the highest binding affinity (Fig. 1*B* and Fig. S2*C*). Therefore, YY146 was selected as the best candidate for in vivo studies.

By using flow cytometry assays, the expression levels of CD146 were determined in two human glioblastoma cell lines: U87MG and U251. Compared with U251 cells, which showed only marginal signal, U87MG cells displayed an enhanced fluorescence indicative of a higher CD146 expression level (Fig. 2*A*). Finally, immunofluorescence micrographs of both tumor cells and tissue revealed strong CD146 staining of the cell membrane in U87MG specimens, but only background levels in U251 tissue (Fig. 2*B*).

PET Tracer Development. To radiolabel YY146 for PET imaging using ^{64}Cu ($t_{1/2}$ of 12.7 h) as the radioisotope, YY146 was conjugated to the chelator 1,4,7-triazacyclononane-triacetic acid (NOTA) using standard activated ester chemistry. Similarly, YY146 was conjugated with an average of one near-infrared dye ZW800 per mAb for near-infrared fluorescence (NIRF) optical imaging. To determine the impact of the chelator on NOTA-YY146 properties, we compared NOTA-YY146 and the unconjugated YY146. Flow cytometry analysis of both U87MG and U251 cells revealed no significant differences in fluorescence intensities between YY146 and NOTA-YY146 (Fig. S3*A*). SDS/PAGE showed no substantial increase in molecular weight of the antibody after conjugation to NOTA (Fig. S3*B*). Consistent with flow cytometry results, fluorescence microscopy examinations of U87MG cells showed comparable CD146 immunofluorescence staining with both YY146 and NOTA-YY146 (Fig. S3*C*). To assess its in vitro serum stability, NOTA-YY146 was incubated with complete mouse serum at physiological temperature for up to 48 h. Flow cytometry analysis

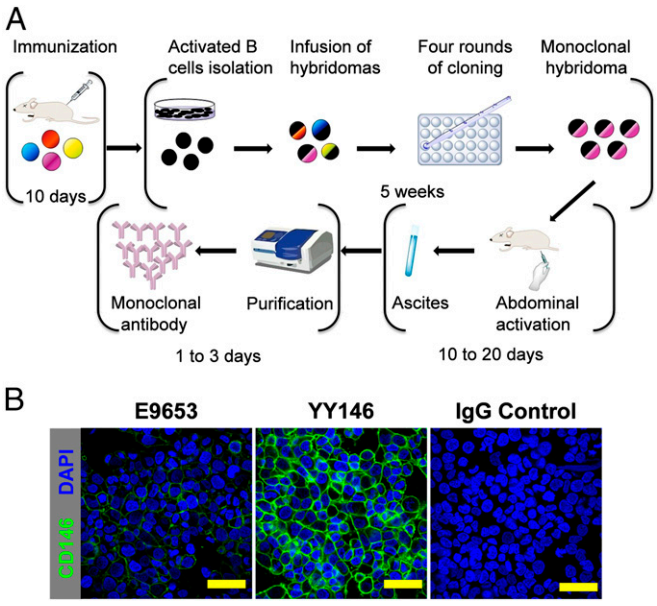

Fig. 1. Modified methodology for the production of anti-human CD146 mAb. (*A*) Schematic representation of the mAb production workflow. A modified protocol was used for the immunization and isolation of activated B cells, which permitted a significant cut in the production time and cost. (*B*) Selection of the most immunoreactive mAb clones. The immunoreactivity of the antibodies was determined by immunofluorescence staining of human melanoma A375 cells, known to overexpress the CD146 antigen; YY146 (clone no. 5) displayed the strongest affinity for the CD146 antigen. (Scale bars: 50 μm.)

revealed no difference in U87MG-binding affinity between treated and control samples, even after prolonged incubation times, evidencing the excellent stability of NOTA-YY146 (Fig. S3*D*). Lastly, the radiolabeling of NOTA-YY146 with ^{64}Cu was accomplished with high yields (>80%), radiochemical purity (>95%), and specific activity (~1.8 GBq/mg).

PET Imaging of CD146 Expression in Subcutaneous U87MG Tumor Xenografts. Small animal PET imaging demonstrated the effectiveness of ^{64}Cu-NOTA-YY146 as a noninvasive imaging agent for the detection of CD146 expression in vivo. As early as 4 h after i.v. administration, tracer uptake in the CD146-overexpressing U87MG s.c. tumor xenografts was readily discernible. Coronal PET images intersecting the tumor showed excellent delineation of the tumor mass with high tumor/muscle contrast, 8.88 ± 0.77 (n = 3) at 48 h after administration of the radiolabeled antibody (Fig. 3*A*). Maximum intensity projection (MIP) images revealed marked hepatic and blood pool accumulation of ^{64}Cu-NOTA-YY146 (Fig. S4). Quantification of radiolabeled antibody uptake in tumor, liver, blood pool, and muscle was performed using a 3D region-of-interest (ROI) analysis of the PET images. (Fig. 3*B* and Table S1). Initially, elevated blood pool and liver activities exhibited a decline over time whereas muscle showed low-level tracer accumulation throughout the longitudinal study. ^{64}Cu-NOTA-YY146 accretion within U87MG tumor increased steadily and reached 13.68 ± 0.66 percent injected dose per gram (%ID/g) at the 48-h postinjection (p.i.) time point. To test the tumor specificity of the tracer, we carried out a CD146 blocking study in which mice were preinjected with a blocking dose (50 mg/kg) of unlabeled YY146, 24 h before ^{64}Cu-NOTA-YY146 infusion. Close to a 70% reduction (P < 0.01) in 48-h p.i. tumor uptake values (13.68 ± 0.66 vs. 5.16 ± 1.50 %ID/g; n = 3) was observed upon blocking, which evidenced the specific character of the ^{64}Cu-NOTA-YY146/CD146 interaction (Fig. 3). Furthermore, mice bearing CD146-negative U251 s.c. xenografts had approximately

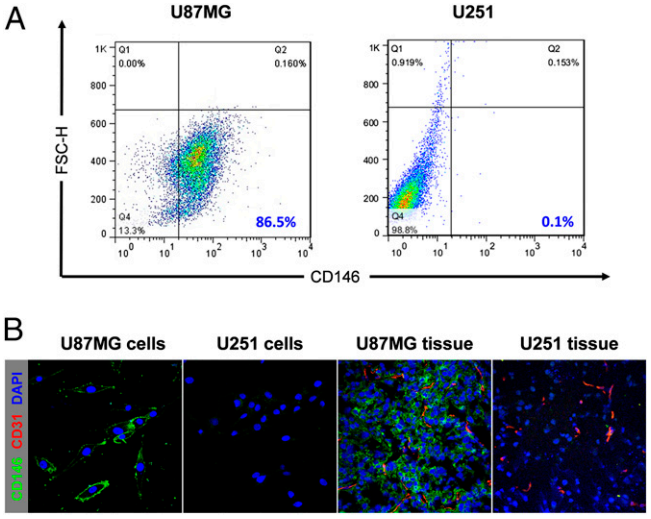

Fig. 2. In vitro characterization of CD146 expression in human cancer cells. (*A*) Flow cytometry of U87MG and U251 human glioblastoma cells. U87MG cells showed markedly higher fluorescence signal, indicative of stronger YY146 binding than U251 cells. (*B*) Immunofluorescence staining of CD146 in U87MG and U251 cells and tissues. Consistently with *A*, U87MG cells and tissue show stronger staining than U251 specimens.

twofold lower tumor uptake values compared with U87MG tumors, at 24-h and 48-h time points. Finally, the activity distribution was similar ($P > 0.05$) (Fig. 3*B*) in the nontarget tissues across the CD146-positive, CD146-negative, and blocking groups.

Ex vivo biodistribution studies were performed after the last imaging time point (48 h p.i.) to confirm accuracy of the PET quantitative data and obtain a more detailed pharmacokinetic profile of the tracer (Fig. 3*C*). The results were in excellent agreement with 48-h p.i. PET-derived biodistribution data. The observed elevated tracer uptakes in blood, liver, and spleen (Table S2) were representative of the typical long circulation half-lives and hepatic clearance of antibodies and their derivatives. Nonspecific uptake in some off-target tissues, such as kidney (~4 %ID/g) was observed at latter time points and reflected the in vivo metabolisms of the tracer. Overall, the ^{64}Cu-NOTA-YY146 biodistribution profile among groups was similar, except for U87MG tumor uptake values that were significantly higher (13.11 ± 1.40 %ID/g, $n = 4$; $P < 0.01$) compared with blocked U87MG and U251 groups, which were 5.83 ± 1.90 and 6.12 ± 2.30 %ID/g, respectively ($n = 4$).

CD146/CD31 immunofluorescence staining of tumor sections validated tracer uptake against in situ CD146 expression. Accordingly, U87MG tumor cells displayed a strong fluorescence signal, in contrast with the marginal levels attained in U251 cells and nontarget tissues, such as muscle (Fig. S5).

PET/CT of Orthotopic Brain Tumor. We generated a more clinically relevant orthotopic tumor model, by stereotactically seeding U87MG or U251 cells into the brain of nude mice, and studied the ability of ^{64}Cu-NOTA-YY146 to detect intracranial malignancies with high specificity. Two weeks after implantation, progression of the orthotopic tumors was monitored using T_2-weighted MRI scans (see Fig. 5). ImmunoPET/computed tomography (CT) and NIRF imaging studies enabled the accurate localization of small tumor nodules (2–3 mm in diameter) in mice bearing MRI-confirmed brain tumors (Fig. 4*A* and Fig. S6). Longitudinal whole body dual-modality PET/CT scanning demonstrated preferential and focal accumulation of the tracer within the tumor mass (Fig. 4*B*). Posterior ROI quantitative analysis of the images revealed a persistently high ^{64}Cu-NOTA-YY146 uptake in CD146-positive U87MG tumors whereas CD146-negative orthotopic U251 displayed a 3.5-fold lower accretion of the radiotracer (21.4 ± 3.54 vs. 6.08 ± 2.09 %ID/g at 48 h p.i., $n = 5$; $P < 0.001$). Interestingly, uptake in orthotopic U87MG tumors was notably greater than in s.c. U87MG xenografts (Fig. 4*C* and Table S1). Negligible activities

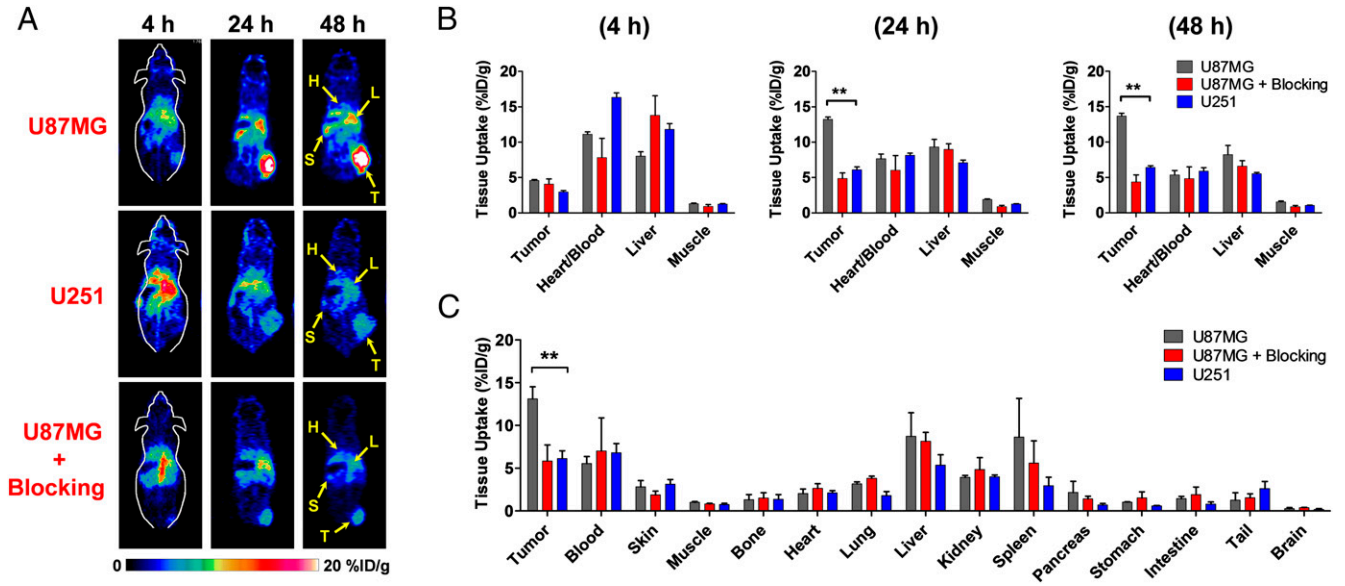

Fig. 3. Noninvasive PET imaging of the in vivo CD146 expression and ex vivo biodistribution of ^{64}Cu-NOTA-YY146 in mice bearing s.c. glioblastoma xenografts. (*A*) Sequential PET images of coronal planes containing s.c. U87MG or U251 tumors. (*Top*) Elevated uptake of the tracer in the U87MG tumor xenografts. Lower tumor uptake was observed in low CD146 expressing U251 tumors (*Middle*) or when U87MG tumor-bearing mice were preinjected with a blocking dose of the unlabeled antibody (*Bottom*). H, heart; L, liver; S, spleen, T, tumor. (*B*) Region of interest (ROI) analysis of the PET images at 4 h, 24 h, and 48 h p.i. showing ^{64}Cu-NOTA-YY146 uptake values in blood pool, liver, muscle, and tumor; values are presented as %ID/g ± SD ($n = 3$ or 4). Tracer accumulation was significantly higher in U87MG xenografts compared with U251 or blocked U87MG groups. (*C*) Ex vivo biodistribution data 48 h after inoculation of the tracer. Mice were euthanized immediately after the last PET scan, and the tissues were collected, weighed, and counted; the results were presented as %ID/g ± SD ($n = 3$ or 4).

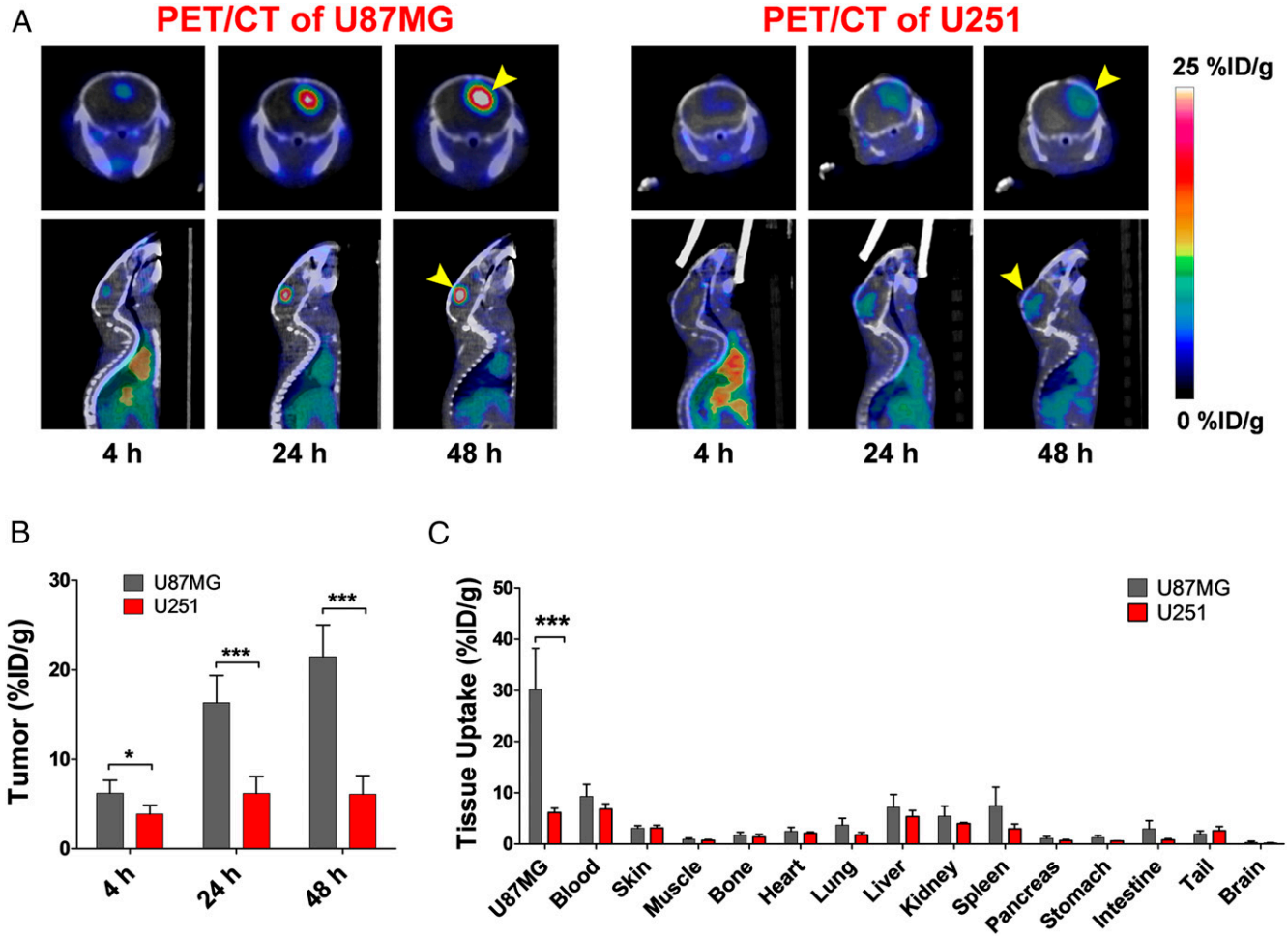

Fig. 4. PET/CT imaging and ex vivo biodistribution studies of ^{64}Cu-NOTA-YY146 in mice bearing orthotopic glioblastoma xenografts. (*A*) Representative sequential PET/CT images of coronal and sagittal planes containing the U87MG or U251 brain tumors. Images revealed a marked accumulation of ^{64}Cu-NOTA-YY146 within U87MG tumor at 4 h, 24 h, and 48 h after injection. (*B*) Comparison of PET ROI-derived quantification of ^{64}Cu-NOTA-YY146 uptake in U87MG (CD146+) vs. U251 (CD146−) tumors. Significantly higher accretion of the tracer in U87MG tumors was observed at 4-h, 24-h, and 48-h time points; reported as %ID/g ± SD ($n = 5$). (*C*) Ex vivo biodistribution of ^{64}Cu-NOTA-YY146 in tumor-bearing mice, 48 h p.i. Uptake in several of the major organs/tissues is presented as %ID/g ± SD ($n = 4$).

were observed in normal areas of the brain surrounding the tumors, which allowed for elevated tumor-to-normal brain contrast ratios of 26.4 and 37.3 in the mice bearing U87MG malignancies, at 24-h and 48-h time points, respectively.

H&E staining of brain sections verified the presence of well-defined tumor masses within the brain, which were consistent with the enhanced signal observed by MRI, NIRF, and PET/CT imaging (Fig. 5). CD146/CD31 immunofluorescence costaining revealed notably stronger CD146 staining of U87MG tumor tissue compared with their U251 counterparts. Additionally, normal brain areas adjacent to the tumors showed lower cell density and background CD146 fluorescence signals (Fig. 5). Ex vivo ^{64}Cu-NOTA-YY146 biodistribution studies at 48 h p.i. resulted in tracer distribution similar to that of the s.c. xenograft models (Fig. 4*C*). We noted a significant discrepancy in U87MG tumor uptake determined by PET quantitative analysis, and the more accurate biodistribution data (21.48 ± 3.54 %ID/g vs. 30.15 ± 8.06 % ID/g, respectively; $n = 4$). This difference was attributed to partial volume effects, known to be the source of a notable underestimation in tracer uptake values when small volumes are analyzed using PET (12). Overall, small animal PET/CT using ^{64}Cu-NOTA-YY146 enabled the highly specific and sensitive detection of aggressive U87MG tumors in the brain.

YY146 Preferentially Targets and Reverts EMT and Cancer Stem Cell Phenotypes. We performed flow cytometry studies to reveal whether CD146 was coexpressed with two of the most common cancer stem cell (CSC) cell markers: CD44 and CD133 (Fig. S7). Overall, CD44 was found to be highly expressed in U87MG cells, and cells with higher CD146 expression levels also displayed the highest CD44 signal. On the other hand, CD133 expression was not detected in U87MG cells. To further demonstrate that YY146 can selectively target a CD146-enriched subpopulation of U87MG cells with EMT and CSC traits using fluorescence-assisted cell sorting (FACS), U87MG cells were sorted into two different subpopulations according to their CD146 expression level: CD146-enriched [termed as U87MG(++)] and CD146 basal [termed as U87MG(+)]. In the two subpopulations, Western blot analysis was performed using a selected panel of proteins, including octamer-binding transcription factor 4 (Oct4), sex-determining region Y-box 2 (Sox2), Nanog, leucine-rich repeat-containing G-protein coupled receptor 5 (LGR5), zinc finger transcription factor (Slug), E-cadherin, protein kinase B (AKT), phosphorylated AKT (p-AKT), and β-Catenin, which are all recognized to be associated with mesenchymal and progenitor cell phenotypes (Fig. 6*A*). Nanog, Oct4, and Sox2, which constitute the core proteins of a transcription complex that maintains

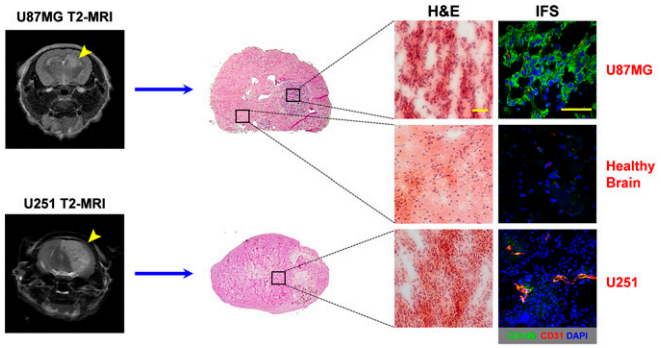

Fig. 5. Histological analysis of glioblastoma tumors obtained from mice bearing MRI-confirmed orthotopic xenografts. T2-weighted MRI shows a distinctive signal enhancement corresponding to the tumor mass. Whole brain coronal tissue sections containing the tumors were prepared for H&E and immunofluorescence (IFS) staining. H&E staining (*Left*) shows the distinctive morphological traits of U87MG and U251 tumors compared with the surrounding normal brain. CD146/CD31 IFS (*Right*) of brain sections revealed a markedly higher CD146 expression (green color) in U87MG tissue whereas U251 and the adjacent normal tissue displayed only low background staining. (Scale bars: 50 μm.)

self-renewal and stemness in human embryonic stem cells (ESCs) (13), were expressed at higher levels in U87MG(++) cells. U87MG(++) cells also showed higher concentrations of LGR5, a protein regarded as a pluripotency marker in stem cells (7). Moreover, a U87MG(++) subpopulation presented distinctive EMT molecular signatures (14), such as low E-cadherin expression levels in conjunction with increased expression of its negative regulator, β-Catenin. These findings hint at the capacity of YY146 to identify and preferentially target cells displaying EMT and stem cell-like phenotypes.

Our next goal was to determine whether treatment with YY146 had a relevant effect on U87MG EMT phenotypes and thus assess its potential therapeutic effect. RT-PCR and Western blot of unsorted U87MG cells incubated for 0 h, 6 h, 12 h, and 24 h with 10 μg/mL YY146 revealed an alteration in the expression levels in several of EMT/CSC-associated markers (Fig. 6 *B* and *C* and Fig. S8). RT-PCR data exposed a time-progressive inhibitory effect on mRNA levels of CD146, which was accompanied by increased transcriptional levels of E-Cadherin. These results perfectly aligned with similar data reported for triple-negative breast cancer, in which the inhibition of CD146 expression with CD146-especific siRNAs led to down-regulation of mesenchymal markers and up-regulation of E-Cadherin (8). Western blot assays further corroborated a decline in the CD146 protein level and its associated increased expression of E-Cadherin, consequently with the changes in their respective transcriptional levels. The restoration of E-Cadherin expression and therefore cell–cell adhesion interaction epitomizes the relevance of CD146 as an EMT inducer and its potential role as an upstream regulator of other relevant EMT genes.

We also observed a reduction of both mRNA and protein levels of Ras-related C3 botulinum toxin substrate 1 (RAC1) upon exposure of U87MG cells to YY146 (Fig. 6 *B* and *C*). RAC1 is a member of the Rho small GTPases family, which regulates mesenchymal motility in U87MG cells, and its inhibition greatly reduces cell invasion (15). Therefore, we explored whether the decline in RAC1 expression translated into the abatement of U87MG cell motility and migratory traits. Transwell invasion assay revealed a marked decline on the invasive and migratory behavior of the treated U87MG cells. The ability of U87MG cells to invade through matrigel membranes was significantly abrogated ($P < 0.01$) when cells were incubated with YY146 (10 μg/mL). On the contrary, a marginal ($P > 0.05$) decrease in migration was observed upon incubation of the cells with an isotype-matched antibody control (Fig. 6*D*). Finally, YY146 cytotoxicity was determined by incubating U87MG cells with increasing amounts of antibody for up to 48 h. Minimal toxicity was observed, with 88.0 ± 7% of cells remaining even after 48 h of incubation with 1 mg/mL YY146 (Fig. 6*E*). These data highlight the exceptional capabilities of YY146 not only to specifically bind to CD146, but also to positively alter EMT-associated mechanisms regulating CSC properties, cell adhesion, motility, and invasiveness in GBM before eliciting significant cell toxicity.

CD146 Expression Correlates with High Grade in Human Gliomas. Given the positive results obtained from in vitro and in vivo experiments, we further investigated the clinical status of CD146 expression in human gliomas. Accordingly, a cohort of 56 patients presenting WHO I to IV grade gliomas was selected with available tissue sections and demographical data (Fig. 7*A*). Semiquantitative immunohistochemical (IHC) analysis of tissue sections, using YY146 as the primary antibody, revealed a higher proportion of CD146-positive staining in WHO grade III and IV tumors compared with grade I and II specimens (Fig. 7*B*). Statistical analysis of the scored samples revealed a statistically significant ($P < 0.05$) correlation between CD146 expression and high WHO grade. In

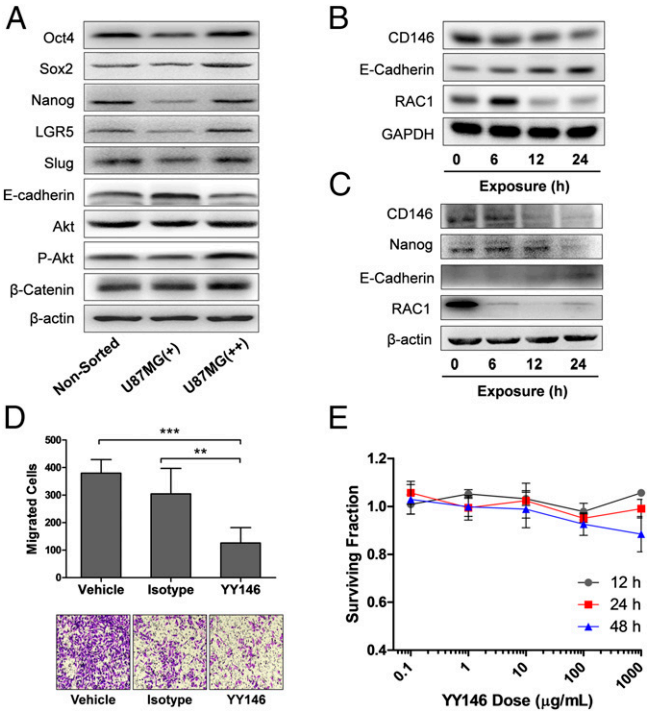

Fig. 6. YY146 preferentially targets stem cell-like tumor cells and reverts their mesenchymal phenotypes. (*A*) Western blot of nonsorted, CD146 low (+) and CD146 high (++) U87MG cell populations. Using FACS, U87MG cells were separated into two population, U87MG(+) and U87MG(++), and the correlation between CD146 levels and the expression of several markers associated with stem cell and mesenchymal phenotypes was determined. The U87MG(++) population displayed marked expression signatures corresponding to stem cell and mesenchymal phenotype. (*B*) RT-PCR of U87MG cells treated with 10 μg/mL YY146 for 0, 6, 12, and 24 h. A decline on the mRNA levels of CD146 and RAC1 was observed whereas E-cadherin was up-regulated upon YY146 treatment. (*C*) Western blots of the YY146-treated cells. Variation on the mRNA levels of CD146, E-cadherin, and RAC1 translated into similar variations on the corresponding protein expression; additionally, a reduction in the expression of Nanog was observed. (*D*) A transwell invasion assay revealed a significant decline in the invasive and migratory behavior of U87MG cells after treatment with YY146, but not in the isotype-matched antibody or vehicle controls. (*E*) YY146 toxicity in U87MG cells. High cell survival was appreciated even after prolonged incubation (48 h) of cells with 1 mg/mL YY146.

A

CD146 clinical status in GBM					
		Negative	Positive	χ^2	P
Age	<40	22	4	0.558	0.455
	>40	23	7		
Gender	F	13	3	0.011	0.915
	M	32	8		
Tumor location	frontal	17	6	1.027	0.311
	non-frontal	28	5		
WHO grade	I	9	1	9.028	0.029
	II	18	2		
	III	12	2		
	IV	6	6		

B

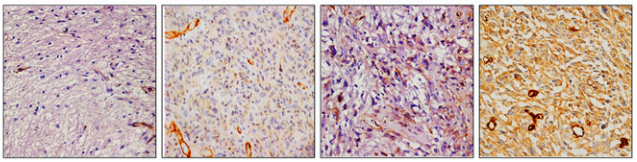

Fig. 7. CD146 expression is associated with human brain cancer histological grade. (*A*) Summary of glioma patient demographics and their corresponding CD146 expression levels. (*B*) IHC staining of CD146 in different WHO grade gliomas. CD146 staining of grades III and IV malignancies is markedly higher (dark brown color) compared with grade I and II tumors.

agreement with the high levels of CD146 expression in human arterial tissue reported by the Genotype-Tissue Expression (GTEx) project, we also noted positive staining of blood vessels. However, the staining of vasculature was notably weaker than that of grade III and IV tumor cells. Overall, these results perfectly aligned with our preclinical observations demonstrating the pathological relevance of CD146 and its potential as a diagnostic, stratification, and therapeutic target of high-grade gliomas (HGG).

Broad Applicability of CD146 and YY146 in Other Solid Tumor Types. Although it was not the primary focus of this study, other solid tumor types were also evaluated for potential YY146 applications. We screened 10 cancer cell lines for CD146 expression using flow cytometry, which included H460 and H358 (lung), SW480 (colon), MD-MB-231 and MCF-7 (breast), SGC-7901 (gastric), CAOV-3 and SKOV-3 (ovary), and HepG2 and Huh-7 (liver). Among those, several expressed high levels of CD146 whereas others were clearly CD146-negative (Fig. S9*A*). These findings suggest that CD46 expression may be useful for potential patient stratification for more efficacious targeted therapies.

We also performed IHC staining pilot studies of several human resected solid tumors of the above mentioned types (gastric carcinoma, ovarian adenocarcinoma, hepatocellular carcinoma, and lung carcinoma) using 19–32 tissue specimens of each type (a total of 91 samples) (Fig. S9 *B* and *C*). Again, YY146 was used as the primary antibody for this study. A markedly stronger CD146 staining was observed in high-grade malignancies, and semiquantitative analysis of the histological data revealed a clear trend of tumors of higher grade to express higher level of CD146 than lower grade tumors. Together, these findings indicated the broad relevance of CD146 in multiple solid tumor types and suggested that YY146 may be used for future diagnostic/therapeutic applications in these tumor types.

Discussion

Given the extremely heterogeneous character of brain cancer, and in particular GBM, there is a need for individualized treatments. This paradigm heavily relies on the identification of predictive biomarkers to provide a clear patient segregation and identify potential responders to a specific targeted therapy (16). Once a target is identified, then a simple, yet robust, standardized clinical test procedure needs to be implemented, not only for patient identification purposes but also for the evaluation of treatment efficacies. Molecular imaging techniques, including PET, are well suited to the task. The PET tracers that have been previously explored for imaging of brain tumors are mainly ^{18}F- or ^{11}C-labeled small molecules targeting aberrant metabolic processes. Antibody-based PET tracers are, in general, superior to small molecules in terms of target specificity and binding affinity. Herein, we demonstrated for the first time, to our knowledge, that expression levels of CD146 can be scrutinized noninvasively in high-grade gliomas with PET imaging for potential patient selection and stratification for targeted therapies.

The value of CD146 in the treatment of malignant melanomas and breast cancer has been previously suggested, and its efficacy as a therapeutic target has been evaluated with encouraging results (7, 17, 18). Therefore, this study was performed to establish and validate CD146 for noninvasive PET imaging of aggressive gliomas. With the implementation of our own modified production approach, we were able to generate YY146, an anti-CD146 monoclonal antibody. This method, which uses activated B cells harvested from popliteal lymph nodes of immunized mice, significantly simplified antigen immunization, B-cell harvesting, and screening processes without compromising the production yields.

Initially, YY146 was radiolabeled with the positron emitter ^{64}Cu, and the ability of ^{64}Cu-NOTA-YY146 to determine tumor burden through the noninvasive acquisition of high-resolution PET images in mice bearing s.c. U87MG tumor xenografts was evaluated. Excellent tumor-to-background ratios were obtained, due to the elevated accretion of the tracer in CD46-positive U87MG tumors and the significantly lower ($P < 0.01$) uptake in the nontarget tissues. Standard methods, such as flow cytometry, RT-PCR, Western blotting, and histological analysis, further demonstrated the correlation between expression of CD146 and tumor uptake. Additionally, antigen-blocking studies demonstrated low nonspecific/background binding of the tracer to blocked U87MG tumors, evidencing the CD146 specificity of ^{64}Cu-NOTA-YY146.

Antibody-based imaging and therapy of brain diseases are greatly challenged by the failure of macromolecules to cross the intact blood–brain barrier (BBB). The poor permeability of the BBB is one of the reasons why systemic therapies, typically effective in other types of cancer, have been less efficacious in treating primary and metastatic brain malignancies (19). However, high-grade gliomas induce several alterations on tumor-associated vasculature, including the formation of fenestrations, disruption of tight junctions, alterations in thickness of the subendothelial basal lamina, and increased perivascular space (20). First line treatment for glioblastomas, which includes maximal surgical resection and radiotherapy, further disrupt the integrity of the BBB (21, 22). Such breakdowns result in enhanced brain permeability to macromolecules and contrast media: e.g., the gadolinium-based MR contrast agent (23).

In this context, antibody-based imaging approaches may be of great utility in diagnostic neurooncology because they may provide superior specificity to distinguish true tumor recurrences from mass effects resulting from standard treatments. Moreover, molecular imaging with antibodies targeting selected tumor-associated antigens may sketch a more accurate picture of the tumor genetic landscape and the heterogeneous spatial distribution of the expression of tumor biomarkers within the tumor bed. This paradigm is of great relevance for better management of HGG patients, given the genotypic and phenotypic heterogeneity of this disease and the lack of clinically amenable noninvasive technologies to assess such inter- and intratumoral variations.

Given the absence of BBB in s.c. brain cancer xenografts and the generally poor resemblance of these models to realistic clinical scenarios (24, 25), we evaluated the targeting properties of ^{64}Cu-NOTA-YY146 in a more appropriate setting. We performed small animal PET/CT and biodistribution studies in orthotopic gliomas to demonstrate the tumor infiltrability of ^{64}Cu-NOTA-YY146. PET/CT images demonstrated the capacity of ^{64}Cu-NOTA-YY146 to penetrate the disrupted BBB and efficaciously target CD146 within U87MG brain tumors. The elevated tumor accumulation of the tracer allowed the acquisition of high contrast PET images that permitted the accurate delineation of very small tumors masses (~2 mm). Conversely, CD146-negative U251 brain xenografts showed significantly lower ($P < 0.001$) tumor uptake compared with U87MG tumors, which demonstrated that high tracer accumulation was CD146-mediated and not an artifact of enhanced permeability and retention (EPR) effects or vascular disruption due to the surgical implantation procedure. Overall, our micro PET/CT and biodistribution studies in orthotopic U87MG and U251 xenografts indicated that ^{64}Cu-NOTA-YY146 is well suited for the CD146-specific imaging of in situ malignant gliomas.

Similar to the radiolabeled mAb, in vivo and ex vivo optical imaging, using fluorescent-labeled ZW800-YY146, also unveiled a high and selective U87MG tumor localization (Fig. S6 *A* and *B*). The clear delineation of orthotopic tumors in the mouse brain using optical imaging suggested that fluorescently labeled YY146, upon future clinical translation, may enable neurosurgeons to completely resect brain tumors in cancer patients via targeted fluorescence image-guided surgery (Fig. S6). In summary, our imaging data indicates the potential of YY146 to selectively recognize CD146 and provide a sensitive method to discern high-grade gliomas from other processes, such as inflammation and necrosis. Along the same line, ^{64}Cu-NOTA-YY146 may offer a means for better patient stratification and the assessment of the response to CD146-targeted therapy. Despite the fact that many hurdles have to be overcome before we can see any clinical application of YY146, our encouraging data prove antibody-based imaging as a relevant tool in diagnostic neurooncology.

The existence of CSC populations, expressing a series of markers (e.g., CD133 and CD44), has been previously reported for high-grade gliomas (26). Being as high as 50% in aggressive GBMs, CSC fractions are thought to be responsible for several clinical hurdles involving GBM aggressiveness, treatment resistance, and relapse (27). Mounting evidence points at EMT as a causal factor in the emergence of CSC phenotypes (28, 29). Additionally, the reversal of EMT/CSC phenotypes to a more differentiated state overexpressing E-Cadherin has been associated with less aggressiveness and increased drug sensitivity (29, 30). Such evidence has led to a justifiable interest in targeting and reverting EMT as a weapon to combat the elusive CSC populations. Flow cytometry studies revealed the existence of a population of U87MG cells expressing high levels of CD146 and CD44 (Fig. S7). Aided by FACS, we isolated CD146-enriched U87MG cells and demonstrated that these subpopulations show increased EMT and CSC traits. First, we observed that U87MG (++) cells presented higher expression of the stem cell markers Oct4, Sox2, Nanog, and LGR5 (27, 31) and exhibited increased levels of both Slug and β-Catenin, overexpression of which have been proven sufficient to repress E-cadherin and drive EMT (8). Further, evaluation of prolonged in vitro exposure to YY146 in U87MG cells indicated that YY146 treatment reduces both mRNA and proteins levels of CD146 and foments the reversal of CSC and EMT phenotypes through the reactivation of E-cadherin expression and abrogation of migratory properties. Deeper investigations are required to understand the mechanisms by which our antibody represses/degrades CD146 and acts on CSC and EMT cell phenotypes; however, those are outside the scope of this work. Taken together, our data shed light on the role of CD146 in determining GBM phenotypical traits and on the promising efficacy of YY146 as a therapeutic agent preferentially targeting extremely aggressive and resistant CSC subpopulations.

Clinical translation of novel agents is a long and very expensive process. Regardless of how promising preclinical data are revealed to be, human trials always will have the last say. Therefore, verifying CD146 expression in human primary gliomas seemed critical. CD146 histopathological analysis of 56 glioma patients of all WHO grades corroborated high expression of the marker in 20% of the cases, with a strong positive staining of 50% of the GBM (WHO grade IV) samples. More importantly, we discovered a statistically significant correlation ($P < 0.05$) of CD146 expression with high tumor grade. Despite being modest, this correlation ratified the feasibility of CD146 to become a suitable molecular target for clinical diagnosis, selection, and stratification of the glioblastoma patient population. In a clinical practice that is constantly evolving toward personalized medicine, YY146-based PET scans may improve GBM clinical outcomes through the identification of the patients (high CD146 expression) who will likely benefit from CD146-targeted molecular therapies (e.g., YY146 alone or in combination with other drugs, radioimmunotherapy, antibody–drug conjugates, etc.) and the monitoring of its early effectiveness. Importantly, not limited to brain tumor, YY146 was also found to have broad applicability in the management of other malignancies outside the CNS, including lung, hepatocellular, and gastric carcinomas.

Materials and Methods

Chemicals and Reagents. AlexaFluor488 and Cy3-labeled secondary antibodies were purchased from Jackson Immunoresearch Laboratories, Inc. Chelex 100 resin (50–100 mesh) and anti-CD146 antibody (E9653) were obtained from Sigma-Aldrich. S-2-(4-Isothiocyanatobenzyl)-1,4,7-triazacyclononane-1,4,7-triacetic acid (p-SCN-Bn-NOTA) was purchased from Macrocyclics, Inc. All aqueous solutions and buffers were prepared using milli-Q grade water (resistivity of >18.2 MΩ•cm) and pretreated with Chelex 100 resin to remove traces of heavy metals. Antibodies for Western blot against β-actin, β-Catenin, and LGR5 were purchased from Santa Cruz Biotechnology, OriGene, and ABCAM, respectively. The rest of the antibodies were provided by Cell Signaling Technologies.

Cell Lines and Animal Models. Human U87MG, U251, and cancer cells were obtained from the American Type Culture Collection (ATCC). U87MG cells were cultured in Dulbecco's modified Eagle medium (Invitrogen) supplemented with penicillin (100 U/mL; Invitrogen), streptomycin (100 μg/mL; Invitrogen), and FBS [10% (wt/vol); Sigma-Aldrich] and incubated at 37 °C in a 5% CO_2 atmosphere. U251 cells were cultured in RPMI 1640 medium (Invitrogen) supplemented with penicillin (100 U/mL; Invitrogen), streptomycin (100 μg/mL; Invitrogen), and FBS [10% (wt/vol); Sigma-Aldrich] and incubated at 37 °C with 5% CO_2. Cells were used for in vitro and in vivo experiments when they reached ~80% confluence.

All animal studies were conducted under a protocol approved by the University of Wisconsin Institutional Animal Care and Use Committee. U87MG and U251 tumor xenografts were induced in 5-wk-old female/male athymic nude mice (Harlan) by s.c. injection of 1×10^6 cells, suspended in 100 μL of a 1:1 mixture of culture medium and Matrigel (BD Biosciences), into the mice lower flank. Tumor size was monitored every other day, and the animals were used for in vivo experiments ~3 wk after implantation, when tumors reached 5–10 mm in diameter. Orthotopic U87MG and U251 brain xenografts were created as described previously (32). Briefly, athymic female nude mice (20–25g) were anesthetized with 3.5% isoflurane and maintained with 2% isoflurane, and the animal's head was scrubbed with an iodine scrub, and then with alcohol, before cell implantation. For implantation, cells were suspended in PBS at a concentration of 1.2×10^4 cells per microliter, and each mouse was stereotactically injected with 7 μL of cell suspension. The injection site was located 2 mm lateral to the sagittal suture, 3 mm posterior to the coronal suture, and 2 mm deep from the surface of the skin. Starting 2 wk postimplantation, the animals were monitored by T2-weighted MRI once a week. Mice with MRI-confirmed brain tumors were used for PET imaging studies.

Antibody Production, Purification, and Cell Screening. Subtractive immunization was used to generate antibodies recognizing human CD146 antigen using a modified method (33). In brief, five mice were immunized via

footpad injection of 100 μg of the human CD146 antigen (Sino Biological Inc.) in Freund's adjuvant medium. Ten days afterward, popliteal lymph nodes of immunized mice were harvested, and B cells were isolated. B cells were fused with SP2/0 mouse myeloma cells and cultured in hypoxanthine, aminopterin, and thymidine (HAT medium). Single hybridoma clones were seeded into wells of 96-well plates by limiting dilution and cultured in fresh HAT medium. The conditioned medium for each clone was screened for anti-CD146 mAb presentation using ELISA. Four rounds of subcloning/screening were performed. The selected clones were cultured in RPMI 1640. Five hundred thousand to 1 million hybridomas were inoculated into Balb/C mice intraperitoneally, and ascites fluid was collected after an average of 2 wk. Monoclonal antibodies were purified from ascites by affinity chromatography (protein G/A columns; GE Healthcare).

ELISA and SDS/PAGE of the Purified Clones. Phage preparations and analysis were done following standard protocols. Briefly, 96-well Maxisorp plates were coated with 1 μg/mL CD146 antigen overnight at 4 °C and subsequently blocked with 2% (wt/vol) BSA at room temperature for 2 h. Antigen-coated wells were incubated for 15 min with different concentrations of antibody. Bound phage was then detected using a horseradish peroxidase (HRP)-conjugated anti-mouse IgG mAb (GE Healthcare). SDS polyacrylamide gel electrophoresis (SDS/PAGE) analysis was performed under nonreducing conditions using 10% (wt/vol) acrylamide gels.

NOTA Conjugation and ^{64}Cu Labeling. Detailed procedures for NOTA conjugation and ^{64}Cu labeling have been reported previously (34). Briefly, ∼3 mg of YY146 in PBS (HyClone) were adjusted to pH 9.0 by addition of Na_2CO_3 (0.1 M), and p-SCN-Bn-NOTA was dissolved in DMSO and immediately added to the antibody solution in a 25:1 molar ratio; pH was readjusted to 9.0, and the reaction was left to proceed for 2 h. NOTA-YY146 was purified using size exclusion PD-10 columns (GE Healthcare) with PBS (pH 7.0) as mobile phase. The conjugation of the near infrared fluorescence dye ZW800-1 to YY146 was accomplished following the above protocol verbatim. High specific activity (>5 Ci/μmol at the end of bombardment) ^{64}Cu was produced in a CTI RDS 112 cyclotron via ^{64}Ni(p,n)^{64}Cu reaction. A radiolabeling reaction was conducted by reacting 50–100 μg of NOTA-YY146 with 74–148 MBq (2-4 mCi) of $^{64}CuCl_2$ in 300 μL of sodium acetate buffer (0.1 M, pH 4.5) at 37 °C for 30 min under constant agitation (500 rpm). ^{64}Cu-NOTA-YY146 was then purified from free activity using PD-10 columns with PBS as the mobile phase. The radioactive fractions containing ^{64}Cu-NOTA-YY146 were collected and filtered through a 0.2-μm filter for in vivo experiments. Radiochemical purity was assessed by radio-instant thin-layer chromatography, mobile phase EDTA, 50 mM (pH 4.5).

Flow Cytometry. The immunoreactivity of YY146, NOTA-YY146, toward U87MG and U251 cells was compared by flow cytometry analysis (35). Briefly, cells were harvested and suspended in cold PBS (pH 7.4) with 2% BSA at a concentration of 1×10^6 cells per milliliter. The cells were incubated with various concentrations of antibody (5 or 25 μg/mL) for 30 min at room temperature, washed three times with cold PBS, and centrifuged at $156 \times g$ for 4 min. After incubation with AlexaFluor488-labeled goat anti-mouse IgG (5 μg/mL) for 30 min at room temperature, the cells were washed and analyzed using a BD FACS Calibur four-color analysis cytometer (Becton-Dickinson) equipped with 488-nm and 633-nm lasers. FlowJo software was used for the analysis and processing on the data (Tree Star, Inc.).

To assess serum stability, NOTA-YY146 was preincubated with complete mouse serum at 37 °C for 0, 24, and 48 h. Afterward, U87MG immunoreactivity was compared among the three samples using flow cytometry, following the procedures described in *Flow Cytometry*.

PET and PET/CT Imaging. Groups (n = 3–5) of athymic nude mice bearing s.c. U87MG, s.c. U251, or orthotopic U87MG tumor xenografts were i.v. administered 5.5–11.1 MBq of ^{64}Cu-NOTA-YY146, and sequential standalone PET or PET/CT scans were acquired at 4, 24, and 48 h postinjection (p.i.). Time points were selected considering the physical half-life of ^{64}Cu (12.7 h) and the typical long circulation times of antibodies (∼100 h) (10). PET and PET/CT studies were performed on an Inveon microPET/microCT rodent model scanner (Siemens Medical Solutions USA, Inc.). Anesthesia was induced with 4% isoflurane and maintained at 2%, and then mice were placed in a prone position in the scanner. To improve image quality, 20 million coincidence events per mouse were acquired for every static PET emission scan (energy window, 350–650 keV; time window, 3.432 ns; resolution, 1.5 mm). For dual modality PET/CT, CT images (80 kV, 900 μA, resolution 105 μm) were obtained, and anatomical registration, as well as attenuation correction, was applied to the correspondent PET scans. To evaluate ^{64}Cu-NOTA-YY146 specificity in vivo, a receptor-blocking study was performed where athymic nude mice bearing s.c. U87MG tumors were preinjected with a blocking dose (100 mg/kg) of the unlabeled YY146, 24 h before administration of ^{64}Cu-NOTA-YY146. Blocked PET images were acquired using the above-described imaging protocol.

Image reconstructions of PET scans were carried out on an Inveon Acquisition Workplace (Siemens Preclinical Solutions) workstation using an ordered subset expectation maximization 3D/maximum a posteriori reconstruction algorithm. Quantitative region-of-interest (ROI) analysis of the PET images was performed on the attenuation and decay corrected PET images using Inveon Research Workplace software (Siemens Preclinical Solutions), and tissue uptake values are presented as the percent injected dose per gram (%ID/g).

MRI. In vivo MRI was performed to monitor tumor growth beginning 2 wk after tumor cell grafting. Anesthesia was induced with 4% isoflurane in compressed air and maintained at 0.5–3%. Animal temperature was maintained with a warm air blower. T2-weighted images were collected using a multislice fast spin echo sequence with the following parameters: repetition time = 3,500 ms; effective echo time = 37.47 ms; echo train length = 8; field of view = 20×20 mm^2, matrix = 256×256, number of excitations = 5, slice thickness = 0.75 mm.

NIRF Imaging. For in vivo whole-body NIRF imaging, mice bearing intracranial U87MG tumors were i.v. injected with ZW800-YY146 (an estimated 400 pmol of the dye). Subjects were then imaged using an IVIS Imaging System (λ_{ex} = 745 nm, λ_{em} = 800 nm) at 3, 24, and 48 h after inoculation of the fluorescence tracer. Mice were then killed at 48 h p.i., and ex vivo NIRF imaging of the major organs was performed.

Ex Vivo Biodistribution. Ex vivo biodistribution studies were performed to demonstrate the accuracy of PET results and to obtain a more complete distribution profile of the tracer. Immediately after the final PET scan at 48 h p.i., mice were euthanized by CO_2 asphyxiation, and blood, tumor, and all major organ/tissues were collected and weighed. The radioactivity of each tissue was counted in an automated γ-counter (Perkin-Elmer), and the tissue accumulations were calculated and reported as %ID/g (mean ± SD).

Confocal Laser Scanning Microscopy. Immunofluorescence staining was conducted to evaluate the expression of CD146 and CD31 following a previously described methodology (35). In a nutshell, tumors from either s.c. or orthotopic sites were collected and embedded in optimal cutting temperature (OCT) compound, frozen, cut into 5-μm tissue slices, and fixed with cold acetone for 10 min. After rinsing with PBS and blocking with 10% donkey serum for 30 min at room temperature, the slices were incubated overnight with a mixture of YY146 (10 μg/mL) and rat anti-mouse CD31 antibody (BD Biosciences) at 4 °C. Primary antibodies were visualized using AlexaFluor488-labeled goat anti-mouse IgG (Invitrogen) and Cy3-labeled donkey anti-rat IgG (The Jackson Laboratory), respectively. Confocal fluorescence images were acquired with a Nikon Digital Eclipse C1 plus microscope equipped with three excitation lasers (488 nm, 546 nm, and 633 nm).

RNA Isolation and RT-PCR. To induce functional responses, U87MG cells were incubated with YY146 (10 μg/mL), and cells were collected at different time points up to 48 h posttreatment for gene expression (calcium assays). Total RNA was extracted and purified from cells using TRIzol reagent (Life Technologies). For determination of the levels of CD146 relevant genes, PCR primers of CD146, Nanog, Oct4, LGR5, and SOX2 were designed by the TaqMan program as follows: CD146, forward, 5′-GCT GCCCAGTGGGAACCACA-3′; reverse, 5′-ATCATGGTGTCCAAGTTCCAGGC-3′; Nanog, forward, 5′-AGGCAA-ACAACCCACTTCT-3′; reverse, 5′-TCACACCATTGCTATTCTTCG-3′; Oct4, forward, 5′-TATTCAGCCAAACGACCATCT-3′; reverse, 5′-TCAGCTTCCTCCACCC-ACTT-3′; Sox2, forward, 5′-ATCACCCACAGCAAATGACA-3′; reverse, 5′-CAAA-GCTCCTACCGTACCACTA-3′; GAPDH, forward, 5′-TGCACCACCAAC TGCTTAGC-3′; reverse, 5′-GGCATGGACTGTGGTCATGAG-3′. An SYBR Green PCR Master Mix (Applied Biosystems) was used, and GAPDH was coamplified as an endogenous control to standardize the amount of the sample RNA. For RT-PCR, total RNA was isolated from U87MG cells using a Qiagen RNeasy Minikit (Qiagen Inc.) and then reverse transcribed and amplified using a Qiagen OneStep RT-PCR kit (Qiagen Inc.). Real-time PCR was performed using TaqMan primers for CD146 (Mm00468256_m1 MCM) and GAPDH (Mm99999915_g1 Gapdh) (Applied Biosystems). RT-PCR conditions were as follows: Hot-start DNA polymerase was activated at 95 °C for 5 min, followed by 35 cycles of 95 °C for 30 s, 55 °C for 30 s, and 72 °C for 30 s . Amplified products were run on a 0.5% agarose gel at 100 V for 1 h and imaged in a Gel Doc EZ imager (Bio-Rad Lab Inc.).

Western Blot. Cells were lysed with radioimmunoprecipitation assay buffer (Beyotime), and total protein concentration was determined with an enhanced bicinchoninic acid (BCA) protein assay kit (Beyotime). Collected cell lysates were mixed with gel-loading buffer, equal amounts of proteins were loaded, separated on 10% SDS/PAGE, and electrophoretically transferred onto nitrocellulose membranes (Millipore), which were blocked in PBS containing Tween 20 (PBST) and 5% milk at room temperature for 2 h and blotted with primary antibody (1:500) overnight at 4 °C. After washing with PBST, the membranes were incubated with anti-mouse horseradish peroxidase-conjugated secondary mAb (1:5,000; Zhongshan Goldenbridge) in PBST containing 5% milk, and immunocomplexes were visualized using the SuperSignal West Dura extended Duration Substrate (34076; Thermo). Images were analyzed by GeneTools image analysis software (SynGene).

U87MG Cell Invasion Assay. To each well of a 24-well plate, 500 μL of DMEM supplemented with 10% FBS were added. Boyden chambers (pore size 8 μm; BD Biosciences) precoated with 2 mg/mL matrigel were then placed atop each of the wells, with the porous membranes in contact with the serum containing media. Next, U87MG cells suspended in serum-free medium containing YY146 (10 μg/mL) were added to the Boyden chamber, and the chambers were incubated in a CO_2 (5%) atmosphere at 37 °C for 24 h. The membranes were removed and washed with PBS, and nonmigrating cells were scraped off using a cotton swab. Migrated cells were fixed with 4% paraformaldehyde and stained with crystal violet. Experiments were performed in triplicate, and the number of invading cells was determined by counting five random fields of view using an inverted light microscope (Leica).

In Vitro Cytotoxicity of YY146. U87MG cells were seeded into 96-well plates at a density of 2×10^5 cells per well and incubated at 37 °C for 12 h, allowing cells to adhere to the plate. Cell media were aspirated, and serial dilutions of YY146 were added to the wells at 0, 0.01, 0.1, 1, 10, 100, and 1,000 μg/mL in 100 μL of media. Cells were allowed to incubate with YY146 for 12, 24, or 48 h. After the incubation time, cell viability was determined using the QBlue Cell Viability Assay Kit (BioChain) using the manufacturer's protocol. In summary, the cell viability reagent was equilibrated to room temperature before 10 μL of reagent was added to each well. The plate was gently shaken to mix the cells with the compound before incubating at 37 °C for 4 h. Fluorescence intensity was measured for each well using a Biotek Synergy 4 plate reader with the 530-nm excitation filter and 590-nm emission filter. Survival fractions were calculated by normalizing the fluorescence of each sample to the unexposed control and plotted against YY146 concentration.

Immunohistochemistry. All specimens were collected during surgery with written informed consents from the patients, and their use for immunohistochemical staining was approved by the Ethics Committee of Southwest Hospital, Third Military Medical University, China. Immunohistochemistry analysis of WHO grade I to IV gliomas and semiquantitative analysis of CD146 expression were performed as previously described using YY146 as the primary antibody (36). Briefly, tumor specimens were surgically removed from patients, and their WHO classification was determined by two or more neuropathologists. Immunostaining was performed using the Envision System with diaminobenzidine (Dako). CD146 expression levels were semiquantitatively scored by two independent pathologists using a visual grading system based on staining intensity and number of positive cells. The percentage of positive cells was evaluated quantitatively. We defined more than 5–25% positive cells as score 1, score 2 for staining of 26–50%, score 3 for staining of 51–75%, and score 4 for staining of >75% of the cancer cells evaluated. Intensity of staining was graded as follows: 0 score for no signal; 1 score for weak; 2 score for moderate; and 3 score for strong staining. Total "staining score" of 0–12 was computed by multiplying the scores of the percentage of positive cells by the scores of the intensity of positive cells. Staining scores of >6 were defined as "positive" whereas staining scores of <6 were considered "negative".

Statistical Analysis. Quantitative data were processed with GraphPad Prism 5.03, and results are expressed as mean ± SD. The correlation of CD146 expression with several clinico-pathological characteristics of the patients was evaluated by χ^2 test using SPSS Statistics 16.0 software. Survival curves were constructed from TCGA data using the Kaplan–Meier method and compared using a log-rank test. Means were compared using an unpaired Student's *t* test, and statistical differences were considered significant if *P* values were less than 0.05 ($*P < 0.05$, $**P < 0.01$, $***P < 0.001$). All groups had a minimum of three subjects ($n \geq 3$).

ACKNOWLEDGMENTS. This work was supported by the University of Wisconsin-Madison, Department of Defense Grants W81XWH-11-1-0644 and W81XWH-11-1-0648, National Science Foundation Grant DGE-1256259, National Institutes of Health, National Institute of Biomedical Imaging and Bioengineering, National Cancer Institute Grants 1R01CA169365, P30CA014520, T32CA009206, and 5T32GM08349, American Cancer Society Grant 125246-RSG-13-099-01-CCE, and Strategic Priority Research Program of the Chinese Academy of Sciences Grant H1808-81201140.

1. Siegel RL, Miller KD, Jemal A (2015) Cancer statistics, 2015. *CA Cancer J Clin* 65(1):5–29.
2. Ostrom QT, et al. (2013) CBTRUS statistical report: Primary brain and central nervous system tumors diagnosed in the United States in 2006-2010. *Neuro-oncol* 15(Suppl 2): ii1–ii56.
3. Omuro A, DeAngelis LM (2013) Glioblastoma and other malignant gliomas: A clinical review. *JAMA* 310(17):1842–1850.
4. Huse JT, Holland EC (2010) Targeting brain cancer: Advances in the molecular pathology of malignant glioma and medulloblastoma. *Nat Rev Cancer* 10(5):319–331.
5. Lehmann JM, Riethmüller G, Johnson JP (1989) MUC18, a marker of tumor progression in human melanoma, shows sequence similarity to the neural cell adhesion molecules of the immunoglobulin superfamily. *Proc Natl Acad Sci USA* 86(24):9891–9895.
6. Ouhtit A, et al. (2009) Towards understanding the mode of action of the multifaceted cell adhesion receptor CD146. *Biochim Biophys Acta* 1795(2):130–136.
7. Wang Z, Yan X (2013) CD146, a multi-functional molecule beyond adhesion. *Cancer Lett* 330(2):150–162.
8. Zeng Q, et al. (2012) CD146, an epithelial-mesenchymal transition inducer, is associated with triple-negative breast cancer. *Proc Natl Acad Sci USA* 109(4):1127–1132.
9. James ML, Gambhir SS (2012) A molecular imaging primer: Modalities, imaging agents, and applications. *Physiol Rev* 92(2):897–965.
10. Holliger P, Hudson PJ (2005) Engineered antibody fragments and the rise of single domains. *Nat Biotechnol* 23(9):1126–1136.
11. Jacobson O, Chen X (2013) Interrogating tumor metabolism and tumor microenvironments using molecular positron emission tomography imaging: Theranostic approaches to improve therapeutics. *Pharmacol Rev* 65(4):1214–1256.
12. Soret M, Bacharach SL, Buvat I (2007) Partial-volume effect in PET tumor imaging. *J Nucl Med* 48(6):932–945.
13. Rodda DJ, et al. (2005) Transcriptional regulation of nanog by OCT4 and SOX2. *J Biol Chem* 280(26):24731–24737.
14. Villarejo A, Cortés-Cabrera A, Molina-Ortíz P, Portillo F, Cano A (2014) Differential role of Snail1 and Snail2 zinc fingers in E-cadherin repression and epithelial to mesenchymal transition. *J Biol Chem* 289(2):930–941.
15. Yamazaki D, Kurisu S, Takenawa T (2009) Involvement of Rac and Rho signaling in cancer cell motility in 3D substrates. *Oncogene* 28(13):1570–1583.
16. Weller M, Stupp R, Hegi M, Wick W (2012) Individualized targeted therapy for glioblastoma: Fact or fiction? *Cancer J* 18(1):40–44.
17. McGary EC, et al. (2003) A fully human antimelanoma cellular adhesion molecule/MUC18 antibody inhibits spontaneous pulmonary metastasis of osteosarcoma cells in vivo. *Clin Cancer Res* 9(17):6560–6566.
18. Mills L, et al. (2002) Fully human antibodies to MCAM/MUC18 inhibit tumor growth and metastasis of human melanoma. *Cancer Res* 62(17):5106–5114.
19. Frank RT, Aboody KS, Najbauer J (2011) Strategies for enhancing antibody delivery to the brain. *Biochim Biophys Acta* 1816(2):191–198.
20. Wolburg H, Noell S, Fallier-Becker P, Mack AF, Wolburg-Buchholz K (2012) The disturbed blood-brain barrier in human glioblastoma. *Mol Aspects Med* 33(5-6):579–589.
21. van Vulpen M, Kal HB, Taphoorn MJ, El-Sharouni SY (2002) Changes in blood-brain barrier permeability induced by radiotherapy: Implications for timing of chemotherapy? (Review). *Oncol Rep* 9(4):683–688.
22. Paganelli G, et al. (2006) Radioimmunotherapy of brain tumor. *Neurol Res* 28(5): 518–522.
23. Chen W (2007) Clinical applications of PET in brain tumors. *J Nucl Med* 48(9):1468–1481.
24. Singh M, Ferrara N (2012) Modeling and predicting clinical efficacy for drugs targeting the tumor milieu. *Nat Biotechnol* 30(7):648–657.
25. Sausville EA, Burger AM (2006) Contributions of human tumor xenografts to anticancer drug development. *Cancer Res* 66(7):3351–3354, discussion 3354.
26. Gaedicke S, et al. (2014) Noninvasive positron emission tomography and fluorescence imaging of CD133+ tumor stem cells. *Proc Natl Acad Sci USA* 111(6):E692–E701.
27. Cruceru ML, Neagu M, Demoulin JB, Constantinescu SN (2013) Therapy targets in glioblastoma and cancer stem cells: Lessons from haematopoietic neoplasms. *J Cell Mol Med* 17(10):1218–1235.
28. Mani SA, et al. (2008) The epithelial-mesenchymal transition generates cells with properties of stem cells. *Cell* 133(4):704–715.
29. Singh A, Settleman J (2010) EMT, cancer stem cells and drug resistance: An emerging axis of evil in the war on cancer. *Oncogene* 29(34):4741–4751.
30. Witta SE, et al. (2006) Restoring E-cadherin expression increases sensitivity to epidermal growth factor receptor inhibitors in lung cancer cell lines. *Cancer Res* 66(2): 944–950.
31. Guo Y, et al. (2011) Expression profile of embryonic stem cell-associated genes Oct4, Sox2 and Nanog in human gliomas. *Histopathology* 59(4):763–775.
32. Tyler B, et al. (2010) A thermal gel depot for local delivery of paclitaxel to treat experimental brain tumors in rats. *J Neurosurg* 113(2):210–217.

33. Grivel JC, et al. (1993) Rapid induction of anti-idiotypic responses to unmodified monoclonal antibodies from syngeneic mice following primary immunization. *J Immunol Methods* 158(2):173–182.
34. Hong H, et al. (2011) Positron emission tomography imaging of CD105 expression during tumor angiogenesis. *Eur J Nucl Med Mol Imaging* 38(7):1335–1343.
35. Yang Y, et al. (2011) In vivo near-infrared fluorescence imaging of CD105 expression during tumor angiogenesis. *Eur J Nucl Med Mol Imaging* 38(11):2066–2076.
36. Shi Y, et al. (2014) Primate-specific miR-663 functions as a tumor suppressor by targeting PIK3CD and predicts the prognosis of human glioblastoma. *Clin Cancer Res* 20(7):1803–1813.